Wang et al. Nanoscale Research Letters (2017) 12:233
DOI 10.1186/s11671-017-2018-8

Nanoscale Research Letters

NANO EXPRESS Open Access

Structural Properties Characterized by the Film Thickness and Annealing Temperature for La_2O_3 Films Grown by Atomic Layer Deposition

Xing Wang, Hongxia Liu*, Lu Zhao, Chenxi Fei, Xingyao Feng, Shupeng Chen and Yongte Wang

Abstract

La_2O_3 films were grown on Si substrates by atomic layer deposition technique with different thickness. Crystallization characteristics of the La_2O_3 films were analyzed by grazing incidence X-ray diffraction after post-deposition rapid thermal annealing treatments at several annealing temperatures. It was found that the crystallization behaviors of the La_2O_3 films are affected by the film thickness and annealing temperatures as a relationship with the diffusion of Si substrate. Compared with the amorphous La_2O_3 films, the crystallized films were observed to be more unstable due to the hygroscopicity of La_2O_3. Besides, the impacts of crystallization characteristics on the bandgap and refractive index of the La_2O_3 films were also investigated by X-ray photoelectron spectroscopy and spectroscopic ellipsometry, respectively.

Keywords: La_2O_3, ALD, Crystallization, Diffusion, Bandgap, Refractive index

Background

During the past decades, lanthanum oxide (La_2O_3) has raised great research interests due to its remarkable chemical, thermal, optical, and electrical properties [1–3]. On the one hand, featuring with high dielectric constant (approximately 27) and large band offsets with silicon (over 2 eV), La_2O_3 is one among the most promising high-k dielectric materials to replace SiO_2 and Si_3N_4 in advanced metal-oxide gate stack in semiconductor devices [4]. Up to now, benefiting from the approach of surface passivation prior to oxide deposition, high-quality ceria/lanthana gate stack suitable for high-k integration in a gate-last process has been accomplished [5]. On the other hand, La_2O_3 is usually used as a kind of effective dopant in thermionic emitters [6], ferroelectric ceramics [7], and oxide catalysts [8], in order to improve properties such as emission capability, effective dielectric constant, and catalytic activity. Besides, La_2O_3 thin films have also received increasing attentions for the various applications in glass ceramic [9], gas sensor [10], supercapacitor [11], etc.

La_2O_3 thin films have been prepared by various physical and chemical deposition methods, such as electron beam evaporation [12], vacuum evaporation [13], chemical vapor deposition [14], atomic layer deposition (ALD) [15], and molecular beam epitaxy [16]. Among the deposition methods mentioned above, due to the nature of the self-limited reaction, ALD has been considered as one of the most promising deposition techniques to produce high quality La_2O_3 thin films with atomic scale thickness controllability, fine uniformity, and excellent conformality [17]. La_2O_3 thin films can be found in several crystalline phases, namely, hexagonal (h-La_2O_3), cubic (c-La_2O_3), amorphous (a-La_2O_3), or a mixture of the phases depending on the film deposition method and post-deposition heat treatment [18]. It is well known that the structural properties of La_2O_3 thin film are determined, to a large extent, by its crystallization and microscopic morphology [19]. Therefore, the study of the crystallization and structure of La_2O_3 thin film is of

* Correspondence: hxliu@mail.xidian.edu.cn
Key Laboratory for Wide-Band Gap Semiconductor Materials and Devices of Education, School of Microelectronics, Xidian University, Xi'an 710071, China

great significance for the compatibility of the film application into advanced electronic devices. In this article, the structural properties of La_2O_3 thin films prepared by ALD technique were investigated by means of a variety of measurements. Attentions were focused on the crystallization conditions of La_2O_3 film and the structural properties characterized by the crystalline states.

Methods

La_2O_3 films were deposited on p-type Si (100) wafers in an atomic layer deposition reactor (Picosun R-150) using $La(^{i\text{-}}PrCp)^3$ as the La precursor while O_3 was used as the oxidant. Prior to deposition of the films, native SiO_2 was removed in a diluted HF solution (1:50). At the deposition temperature of 300 °C, a steady-state growth rate of ~0.85 Å/cycle is obtained by optimizing the process parameters (0.1 s $La(^{i\text{-}}PrCp)_3$ pulse/4 s purge with N_2/0.3 s O_3 pulse/10 s purge with N_2). Ten and twenty nanometer La_2O_3 films were prepared by varying the number of ALD cycles. For both the 10 and 20 nm La_2O_3 films, post-deposition rapid thermal annealing (RTA) was carried out at 400, 600, and 800 °C for 60 s in vacuum ambient (~1 mbar). The ellipsometric spectra of La_2O_3 films were measured before and after annealing by spectroscopic ellipsometry (SE) system (J.A.Woollam Co. M2000U, Lincoln, NE, USA) over the wavelength range from 245 to 1000 nm. In order to address the evolution of the crystallographic structure, grazing incidence X-ray diffraction (GIXRD) measurements were carried out at an angle of incidence of 1° on both the as-grown and annealed La_2O_3 films. Cross-sectional high-resolution transmission electron microscopy (HRTEM) and energy-dispersive X-ray spectroscopy (EDX) line scan measurements were performed with [100] direction of the Si substrate to observe the microstructures and atomic compositions of the La_2O_3 films. X-ray photoelectron spectroscopy (XPS) analysis on a Theta 300 XPS system from Thermo Fisher was employed to investigate the bandgaps of the deposited films. After being exposed to air in clean room environment with a relative humidity of 50% for 48 h, GIXRD and HRTEM measurements were carried out on the as-grown and annealed La_2O_3 films again for further analysis.

Results and Discussion

Figure 1 illustrates the GIXRD analysis performed on the as-grown and annealed La_2O_3 films. The powder patterns of h-La_2O_3 [20] and h-$La(OH)_3$ [21] are added for comparison. As the GIXRD measurements were carried out immediately after the deposition and annealing process, no peaks attributed to $La(OH)_3$ exist in the GIXRD diffractograms. The 10 nm La_2O_3 film (as shown in Fig. 1a) shows no diffraction features before and after a 400 °C annealing treatment, suggesting an amorphous disordered structure of the film. After being annealed at 600 and 800 °C, only weak crystalline planes such as hexagonal (101) appear [22, 23], indicating the impossibility of converting the 10 nm La_2O_3 film into complete crystalline phase. The very small and broad peak around 50° in the diffractogram of the 10 nm La_2O_3 film annealed at 800 °C does not fit to the h-La_2O_3 or h-$La(OH)_3$ patterns. We think it may be formed under the influence of several crystalline planes of h-La_2O_3 around 50°. However, for the 20 nm La_2O_3, the as-grown film already shows a small degree of crystallinity with a couple of peaks attributed to h-La_2O_3 (as shown in Fig. 1b). After being annealing treated, the intensities of the GIXRD peaks increase, which means the enhancement in the degree of crystallinity. After annealing at 600 °C, except for the weak cubic (332) plane [14], the film was mainly crystallized to hexagonal phase as the GIXRD diffractograms exhibit strong hexagonal planes such as (101), (102), (103), and

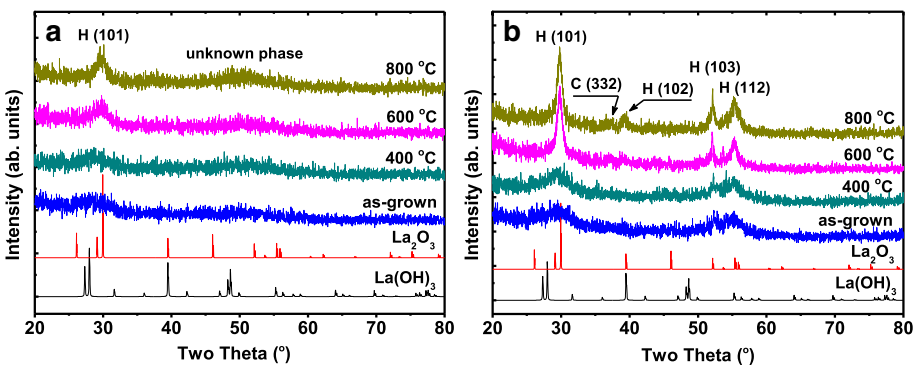

Fig. 1 GIXRD diffractograms of as-grown and annealed La_2O_3 films deposited on Si substrate. **a** 10 and **b** 20 nm La_2O_3 films. Hexagonal La_2O_3 and hexagonal $La(OH)_3$ patterns are added for comparison

(112). Besides, further increase in the annealing temperature up to 800 °C does not seem to significantly affect the GIXRD diffractograms of the film. That is, upon 600 °C, the increase in the annealing temperature does not enhance the crystallinity of the film. Consequently, when annealed upon 600 °C, an almost complete crystallization could be accomplished for the 20 nm La_2O_3 film.

Additional structural information at the La_2O_3/Si interface after RTA treatment at 600 °C is provided by HRTEM-EDX analysis as shown in Fig. 2. For both 10 nm (Fig. 2a) and 20 nm (Fig. 2b) La_2O_3 films, the lanthanum and oxygen in-depth distributions in the EDX elemental ratio profiles show a parallel profile and the La/O ratio is close to 2:3 which meets well with the stoichiometry of La_2O_3. In the HRTEM images, an amorphous region between the Si substrate and the fabricated film, corresponding to an interfacial layer (IL) formed during the ALD growth and RTA process [24], could be found in both Fig. 2a, b. After the amorphous IL, it is possible to identify a region containing nanometer-sized crystals in the 10 nm La_2O_3 film, indicating the existence of an incomplete structural conversion (from amorphous to crystallographic structure) during the RTA treatment. However, the structure of the 20 nm La_2O_3 film is a little complicated. With the guidance of dotted lines, an amorphous region, a nanometer-sized crystal transition region, and a long-range ordered crystal region could be observed in the HRTEM image of Fig. 2b. The presence of long-range ordered crystals manifests, in accordance with the GIXRD results shown in Fig. 1, that RTA process upon 600 °C induces an almost complete crystallization of the 20 nm La_2O_3 film.

It is worth noting that upon the same annealing condition of at 600 °C for 60 s in vacuum ambient (~1 mbar), the 10 and 20 nm La_2O_3 films show different crystalline characteristics. We attribute this difference to the RTA-induced Si diffusion from the substrate into the La_2O_3 layer [25]. As we know, La_2O_3 exhibits the highest affinity for Si atoms among the rare-earth oxide films due to the so called "lanthanide contraction" property of rare-earth elements [26]. Even in the as-deposited La_2O_3 film grown by ALD method, substrate silicon atoms diffuse moderately and distribute in gradient from Si substrate to the upper layer, causing the presence of an IL about 1 nm [27, 28]. Besides, part of the as-deposited La_2O_3 film close to the IL could be considered as Si-riched and difficult to crystallize as Si rich help to prevent the formation of crystalline La_2O_3 precipitates [29]. Furthermore, post-deposition annealing causes extra silicon out diffusion and reaction with excess oxygen in the film. Consequently, in thin La_2O_3 film with the thickness of 10 nm or less, during the annealing process, the substrate Si atoms would diffuse deep easily to the upper layer before the film is crystallized. However, for the 20 nm as-deposited La_2O_3, since Si atoms distribute in gradient from Si substrate to the upper layer, a great part of the film relatively far away from Si substrate is pure. We think that this part of La_2O_3 film could be crystallized at appropriate post-deposition treatment such as RTA carried out at 600 and 800 °C for 60 s in vacuum ambient (~1 mbar) in this work. Crystallization of the film brings in an aggressive enhancement in the packing density and thermodynamic stability. Thus, to a certain extent, the diffusion of Si atoms from substrate into the upper layer would be restrained. As a result, the silicate layer of the 20 nm La_2O_3 film is slightly thinner than what could be observed in the 10 nm La_2O_3 film. Besides, in the 20 nm La_2O_3 film, only 3~4 nm La_2O_3 closed to the IL was converted into nanometer-sized crystals under the influence of Si diffusion during the annealing process. Complete crystallization of the as-

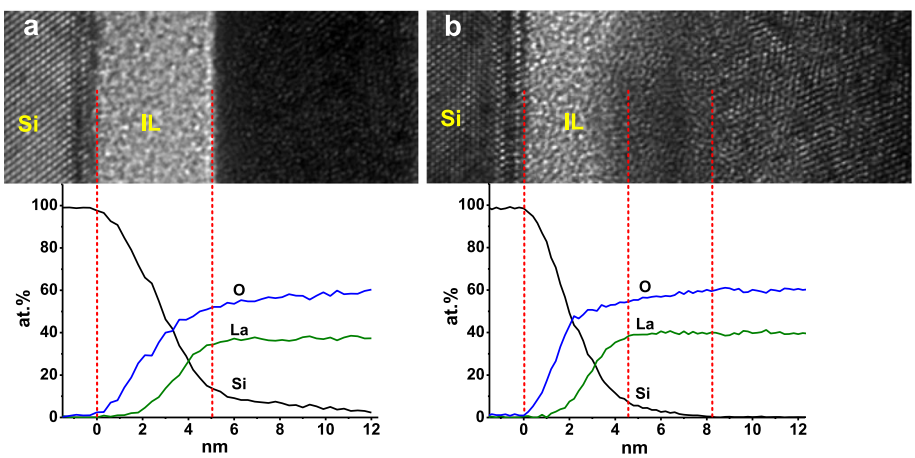

Fig. 2 HRTEM images and EDX profiles near the interface for La_2O_3 films annealed at 600 °C. **a** 10 and **b** 20 nm La_2O_3 films

grown film into the h-La_2O_3 phase is achieved in the region not affected by Si diffusion.

The bandgaps of the as-grown and annealed (at 600 °C) La_2O_3 films were measured by examining the energy loss of the O 1s core levels as shown in Fig. 3. As we know, the bandgap equals the energy distance between the photoemission peak centroid and the onset of the features due to single particle excitations, and it is usually obtained from the inelastic energy loss features observed on the high binding energy side of the core level photoemission peaks [30]. The onset of O 1s loss spectrum was determined by linearly extrapolating the segment of maximum negative slope to the back ground level [31]. The bandgaps of the as-grown 10 and 20 nm La_2O_3 films are determined to be 5.55 and 5.45 eV, respectively. These values are in fairly good agreement with Ohmi et al. [32], who have reported a bandgap of 5.50 eV for non-crystallized La_2O_3 on Si substrate. The bandgap of the annealed 20 nm La_2O_3 film is determined to be 5.20 eV, which agrees well with the bandgap of 5.30 eV for crystallized La_2O_3 reported by Zhao et al. [33]. However, the diffusion of Si during the annealing process brings in large mounts of La-O-Si bonds for the 10 nm La_2O_3, leading to the increase of the inelastic energy loss during the transition from valence band to conduction band, which means the increment of bandgap [34]. As a result, the bandgap of the annealed 10 nm La_2O_3 is figured out as 6.0 eV, which is evidently larger than the bandgap of crystallized La_2O_3.

Figure 4 illustrates the annealing temperature dependence of refractive indexes for the as-grown and annealed La_2O_3 films revealed by SE fitting. The refractive indexes of the La_2O_3 films were determined by fitting the ellipsometry data using the well-known Tauc-Lorentz dispersion mode, which was proposed by Jellison and Modine and has been successfully applied to a variety of amorphous and crystallized materials [35–37]. As revealed in Fig. 4, the refractive indexes of the as-grown La_2O_3 films increase with varying degrees after being annealed at different temperatures. It was reported that the refractive index is closely related to the density of materials, being lower at lower density. Consequently, the increase in the refractive index is caused by the stress release and densification during the annealing process [38, 39]. Furthermore, for the 20 nm La_2O_3 film, an abrupt increase in the refractive index could be observed when the annealing temperature increased from 400 to 600 °C, indicating an aggressive enhancement in the packing density upon crystallization. As a result, after being annealed at 600 °C, the 20 nm La_2O_3 film shows an index of refraction of 1.943 at the wavelength of 632.8 nm, which is much higher than that of the as-grown film (1.838). The

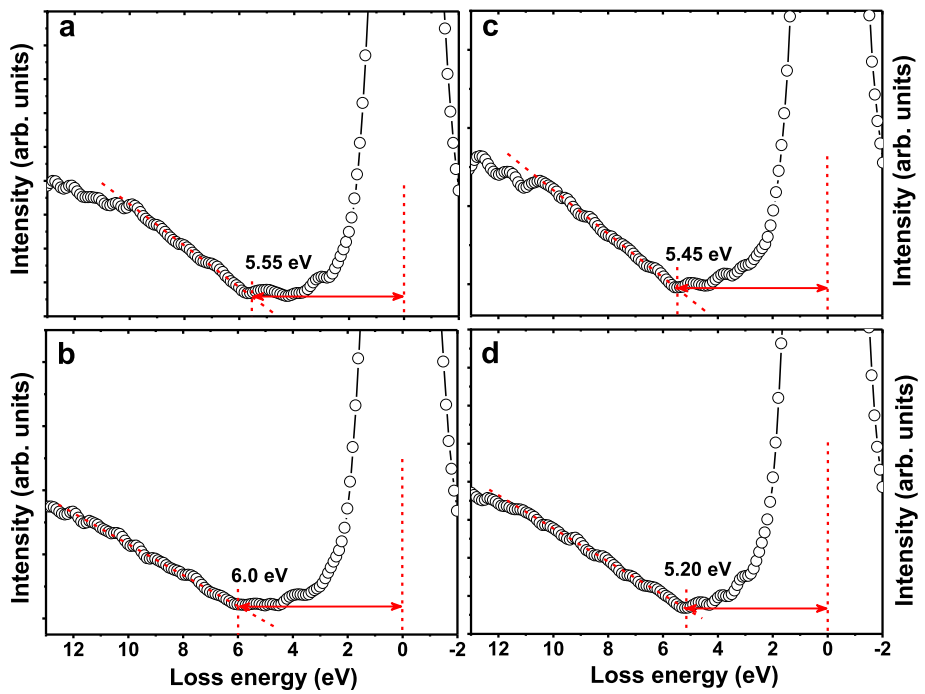

Fig. 3 Bandgaps for the La_2O_3 films with different thickness and annealing temperatures. **a** as-grown 10 and **b** 10 nm La_2O_3 annealed at 600 °C, and **c** as-grown 20 and **d** 20 nm La_2O_3 annealed at 600 °C

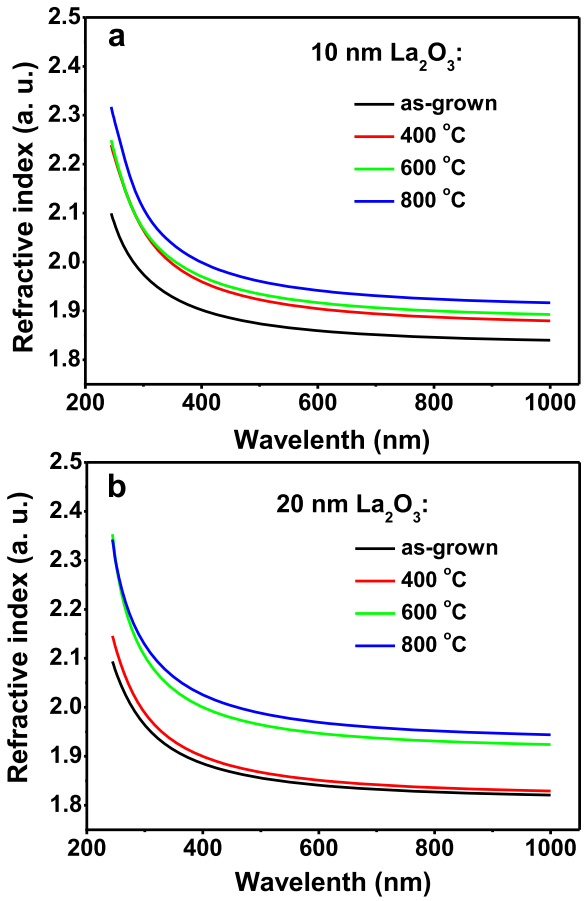

Fig. 4 Annealing temperature dependence of refractive index for ALD-La_2O_3 with different thickness. **a** 10 nm La_2O_3 films and **b** 20 nm La_2O_3 films

refractive indexes obtained in this work are of good comparability with the results reported by Armelao et al. [1] and Kukli et al. [40].

Figure 5 illustrates the GIXRD diffractograms for the as-grown and annealed La_2O_3 films after being exposed to air in clean room environment with a relative humidity of 50% for 48 h. Compared with the GIXRD diffractograms obtained before the air exposure as displayed in Fig. 1, almost all the GIXRD peaks attributed to *h*-La_2O_3 disappear, whereas new peaks attributed to *h*-$La(OH)_3$ appear due to the hygroscopicity of La_2O_3 [22, 23, 41]. It is noteworthy that strong *h*-$La(OH)_3$ phase peaks are only found in the well crystallized samples such as the 20 nm La_2O_3 films annealed at 600 and 800 °C, while few weak peaks are observed in the amorphous disordered and nanometer-sized crystallographic samples. Besides, it seems that the air exposure has a much heavier effect on the 20 nm La_2O_3 than that on the 10 nm La_2O_3. For clarity, cross-sectional HRTEM measurements on the annealed 10 and 20 nm La_2O_3 films after the air exposure were performed. The cross-sectional HRTEM image of the annealed 20 nm La_2O_3 after being exposed to air is shown in Fig. 6b, in which much more uneven interface and surface are observed than what can be found in the 10 nm La_2O_3. The deteriorations in the interface and surface properties are attributed to the degradation in the film density caused by the conversion from *h*-La_2O_3 to *h*-$La(OH)_3$. With the time exposed to air, the amount of $La(OH)_3$ in La_2O_3 film increases and then the density of the film is degraded, resulting in the changes of the surface and interfacial morphologies [42]. However, the existence of large mounts of LaSiO in the 10 nm La_2O_3 enhances the stability of the film structure, providing a high immunity against moisture ambient.

Conclusions

The crystallization of La_2O_3 film grown by atomic layer deposition on Si substrate is restricted by the thickness of the film and the post-deposition annealing temperature. For thin (~10 nm) La_2O_3 film, only nanometer-sized crystals are formed after the annealing treatment due to the diffusion of Si substrate. For

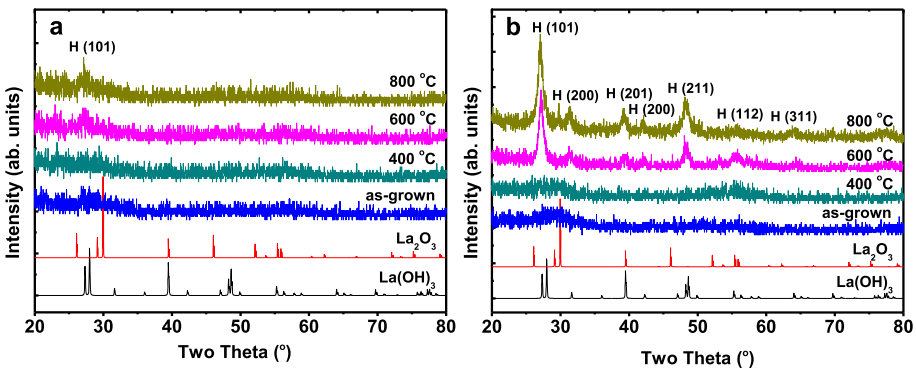

Fig. 5 GIXRD diffractograms for as-grown and annealed La_2O_3 after being exposed to air for 48 h. **a** 10 nm La_2O_3 films annealed at 600 °C and **b** 20 nm La_2O_3 films annealed at 600 °C. Hexagonal La_2O_3 and hexagonal $La(OH)_3$ patterns are added for comparison

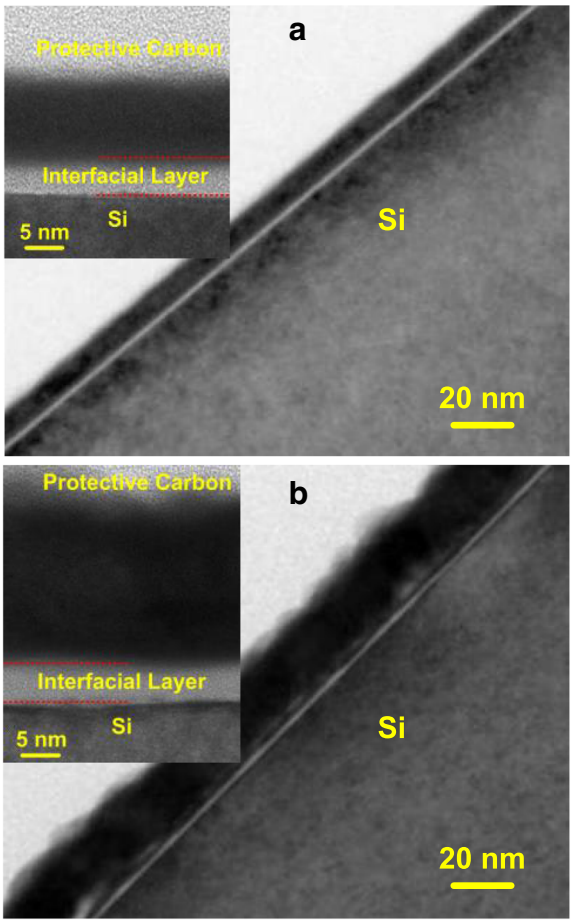

Fig. 6 HRTEM images for the annealed La_2O_3 films after being exposed to air for 48 h. **a** 10 nm La_2O_3 film annealed at 600 °C and **b** 20 nm La_2O_3 film annealed at 600 °C

thick (~20 nm) La_2O_3, films can be mainly crystallized into *h*-La_2O_3 upon RTA performed in vacuum environment at 600 °C. After being crystallized, the refractive index of La_2O_3 film increases dramatically, while the bandgap is slightly decreased. After an exposure to air for 48 h, the *h*-La_2O_3 films are converted into *h*-$La(OH)_3$ due to the hygroscopicity of La_2O_3.

Abbreviations

ALD: Atomic layer deposition; EDX: Energy dispersive X-ray spectroscopy; GIXRD: Grazing incidence X-ray diffraction; HRTEM: High-resolution transmission electron microscopy; IL: Interfacial layer; RTA: Rapid thermal annealing; SE: Spectroscopic ellipsometry; XPS: X-ray photoelectron spectroscopy

Funding

The authors gratefully acknowledge the financial supports for this work from the National Natural Science Foundation of China (grant nos. 61376099 and 61434007) and the Foundation for Fundamental Research of China (grant no. JSZL2016110B003). The National Natural Science Foundation of China and the Foundation for Fundamental Research of China did neither participate in the design of the study nor in the collection, analysis, and interpretation of data or the writing of the manuscript. We are very grateful to Dr. Yanlin Pan for the valuable assistance and excellent technical support for the HRTEM-EDX measurements.

Authors' Contributions

XW generated the research idea, analyzed the data, and wrote the paper. XW and LZ carried out the experiments and measurements. XyF and CxF participated in the discussions. SpC and YtW gave kind suggestions about the experiments and measurements. HxL has given final approval of the version to be published. All authors read and approved the final manuscript.

Authors' Information

XW, LZ, and CxF are PhD students in Xidian University. HxL is a professor in Xidian University. XyF and YtW are Master students in Xidian University.

Competing Interests

The authors declare that they have no competing interests.

Publisher's Note

Received: 3 December 2016 Accepted: 20 March 2017
Published online: 29 March 2017

References

1. Armelao L, Pascolini M, Bottaro G, Bruno G, Giangregorio MM, Losurdo M, Malandrino G, Lo Nigro R, Fragalà ME, Tondello E (2009) Microstructural and optical properties modifications induced by plasma and annealing treatments of lanthanum oxide sol–gel thin films. J Phys Chem C 113:2911–2918
2. Wei C, Fan JL, Gong HR (2015) Structural, thermodynamic, and mechanical properties of bulk La and A-La_2O_3. J Alloy Compd 618:615–622
3. Richard D, Errico LA, Rentería M (2015) Electronic, structural, and hyperfine properties of pure and Cd-doped hexagonal La_2O_3 semiconductor. Comp Mater Sci 102:119–125
4. Kim WH, Maeng WJ, Moon KJ, Myoung JM, Kim H (2010) Growth characteristics and electrical properties of La_2O_3 gate oxides grown by thermal and plasma-enhanced atomic layer deposition. Thin Solid Films 519:362–366
5. Flege JI, Kaemena B, Schmidt T, Falta J (2014) Epitaxial, well-ordered ceria/lanthana high-k gate dielectrics on silicon. J Vac Sci Technol B 32(3):03D124
6. Hoebing T, Hermanns P, Bergner A, Ruhrmann C, Traxler H, Wesemann I, Knabl W, Mentel J, Awakowicz P (2015) Investigation of the flickering of La_2O_3 and ThO_2 doped tungsten cathodes. J Appl Phys 118:023306
7. Wei LL, Yang ZP, Chao XL, Jiao H (2014) Structure and electrical properties of $Ca_{0.28}Ba_{0.72}Nb_2O_6$ ceramics with addition of rare earth oxides (CeO_2, La_2O_3). Ceram Int 40:5447–5453
8. Wang N, Liu JJ, Gu WW, Song Y, Wang F (2016) Toward synergy of carbon and La_2O_3 in their hybrid as an efficient catalyst for the oxygen reduction reaction. RSC Adv 6:77786–77795
9. Yoshimoto K, Masuno A, Inoue H, Watanabe Y (2012) Transparent and high refractive index La_2O_3–WO_3 glass prepared using containerless processing. J Am Ceram Soc 95(11):3501–3504
10. Ehsani M, Hamidon MN, Toudeshki A, Shahrokh Abadi MH, Rezaeian S (2016) CO_2 gas sensing properties of screen-printed La_2O_3/SnO_2 thick film. IEEE Sens J 16(18):6839–6845
11. Yadav AA, Kumbhar VS, Patil SJ, Chodankar NR, Lokhande CD (2016) Supercapacitive properties of chemically deposited La_2O_3 thin film. Ceram Int 42:2079–2084
12. Wong H, Yang BL, Kakushima K, Ahmet P, Iwai H (2012) Effects of aluminum doping on lanthanum oxide gate dielectric films. Vacuum 86:929–932
13. Dakhel AA (2007) Structural and ac electrical properties of oxidized La and La–Mn thin films grown on Si substrates. Mater Chem Phys 102:266–270
14. Kim HJ, Jun JH, Choi DJ (2008) Characteristics of La_2O_3 thin films deposited using metal organic chemical vapor deposition with different oxidant gas. Ceram Int 34:953–956
15. Wiemer C, Lamagna L, Fanciulli M (2012) Atomic layer deposition of rare-earth-based binary and ternary oxides for microelectronic applications. Semicond Sci Technol 27:074013
16. Kakushima K, Tachi K, Ahmet P, Tsutsui K, Sugii N, Hattori T, Iwai H (2010) Advantage of further scaling in gate dielectrics below 0.5 nm of equivalent oxide thickness with La_2O_3 gate dielectrics. Microelectron Reliab 50:790–793
17. Yang W, Sun QQ, Fang RC, Chen L, Zhou P, Ding SJ, Zhang DW (2012) The thermal stability of atomic layer deposited $HfLaO_x$: material and electrical characterization. Curr Appl Phys 12:1445–1447

18. Ramana CV, Vemuri RS, Kaichev VV, Kochubey VA, Saraev AA, Atuchin VV (2011) X-ray photoelectron spectroscopy depth profiling of La_2O_3/Si thin films deposited by reactive magnetron sputtering. ACS Appl Mater Inter 3:4370–4373
19. Song JB, Lu CH, Xu D, Ni YR, Liu YJ, Xua ZZ, Liu JX (2010) The effect of lanthanum oxide (La_2O_3) on the structure and crystallization of poly (vinylidene fluoride). Polym Int 59:954–960
20. Inorganic Crystal Structure Database (2009) Fachinformationszentrum, Karlsruhe., file No. 24693
21. Inorganic Crystal Structure Database (2009) Fachinformationszentrum, Karlsruhe., file No. 31584
22. Hu CG, Liu H, Dong WT, Zhang YY, Bao G, Lao CS, Wang ZL (2007) $La(OH)_3$ and La_2O_3 nanobelts—synthesis and physical properties. Adv Mater 19:470–474
23. Aghazadeh M, Arhami B, MalekBarmi AA, Hosseinifard M, Gharailou D, Fathollahi F (2014) $La(OH)_3$ and La_2O_3 nanospindles prepared by template-free direct electrodeposition followed by heat-treatment. Mater Lett 115:68–71
24. Lee WJ, Ma JW, Bae JM, Kim CY, Jeong KS, Cho MH, Chung KB, Kim H, Cho HJ, Kim DC (2013) The diffusion of silicon atoms in stack structures of La_2O_3 and Al_2O_3. Curr Appl Phys 13:633–639
25. Park TJ, Sivasubramani P, Wallace RM, Kim J (2014) Effects of growth temperature and oxidant feeding time on residual C- and N-related impurities and Si diffusion behavior in atomic-layer-deposited La_2O_3 thin films. Appl Surf Sci 292:880–885
26. Ono H, Katsumata T (2001) Interfacial reactions between thin rare-earth-metal oxide films and Si substrates. Appl Phys Lett 78:13
27. Lamagna L, Wiemer C, Perego M, Volkos SN, Baldovino S, Tsoutsou D, Schamm-Chardon S, Coulon PE, Fanciulli M (2010) O_3-based atomic layer deposition of hexagonal La_2O_3 films on Si (100) and Ge (100) substrates. J Appl Phys 108:084108
28. Kim H, Woo S, Lee J, Kim H, Kim Y, Lee H, Jeon H (2010) The effects of annealing ambient on the characteristics of La_2O_3 films deposited by RPALD. J Electrochem Soc 157:H479–H482
29. Wilka GD, Wallace RM (1999) Electrical properties of hafnium silicate gate dielectrics deposited directly on silicon. Appl Phys Lett 74:2854–2856
30. Bell FG, Ley L (1988) Photoemission study of SiO_x ($0 \le x \le 2$) alloys. Phys Rev B 37:8383–8393
31. Liu QY, Fang ZB, Liu SY, Tan YS, Chen JJ (2014) Band offsets of La_2O_3 films on Ge substrates grown by radio frequency magnetron sputtering. Mater Lett 116:43–45
32. Ohmi S, Kobayashi C, Kashiwagi I et al (2002) Characterization of La_2O_3 and Yb_2O_3 thin films for high-k gate insulator application. Electrochem Soc 150(7):F134–F140
33. Zhao Y, Kita K, Kyuno K, Toriumi A (2009) Band gap enhancement and electrical properties of La_2O_3 films doped with Y_2O_3 as high-k gate insulator. Appl Phys Lett 94:042901
34. Zhang F, Saito K, Tanaka T, Nishio M, Arita M, Guo Q (2014) Wide bandgap engineering of $(AlGa)_2O_3$ films. Appl Phys Lett 105:162107
35. Jellison GE Jr, Modine FA (1996) Parameterization of the optical functions of amorphous materials in the interband region. Appl Phys Lett 69:371–373
36. He G, Zhu LQ, Liu M, Fang Q, Zhang LD (2007) Optical and electrical properties of plasma-oxidation derived HfO_2 gate dielectric films. Appl Surf Sci 253:3413–3418
37. Giannakopoulou T, Todorova N, Giannouri M, Yu J, Trapalis C (2014) Optical and photocatalytic properties of composite TiO_2/ZnO thin films. Catal Today 230:174–180
38. Wang ZY, Zhang RJ, Lu HL, Chen X, Sun Y, Zhang Y, Wei YF, Xu JP, Wang SY, Zheng YX, Chen LY (2015) The impact of thickness and thermal annealing on refractive index for aluminum oxide thin films deposited by atomic layer deposition. Nanoscale Res Lett 10:46
39. Nayar P, Khanna A, Kabiraj D, Abhilash SR, Beake BD, Losset Y, Chen BH (2014) Structural, optical and mechanical properties of amorphous and crystalline alumina thin films. Thin Solid Films 568:19–24
40. Kukli K, Ritala M, Pore V, Leskelä M, Sajavaara T, Hegde RI, Gilmer DC, Tobin PJ, Jones AC, Aspinall HC (2006) Atomic layer deposition and properties of lanthanum oxide and lanthanum-aluminum oxide films. Chem Vap Deposition 12:158–164
41. Calmels L, Coulon PE, Schamm-Chardon S (2011) Calculated and experimental electron energy-loss spectra of La_2O_3, $La(OH)_3$, and LaOF nanophases in high permittivity lanthanum-based oxide layers. Appl Phys Lett 98:243116
42. Zhao Y, Toyama M, Kita K, Kyuno K, Toriumi A (2006) Moisture-absorption-induced permittivity deterioration and surface roughness enhancement of lanthanum oxide films on silicon. Appl Phys Lett 88:072904